Two-Step Wetting of Nanoporous Carbons: Small Angle Scattering Analysis of Capillary Rise

François Chaltin,[†] Martin Rosenthal,[‡,¶] Alexandre F. Léonard,[§] Bart Goderis,[¶] and Cedric J. Gommes[*,†]

[†]*Department of Chemical Engineering, University of Liège B6A, Allée du Six Août 13, 4000 Liège, Belgium*

[‡]*Dual-Belgian-Beamline (DUBBLE, BM26), European Synchrotron Radiation Facility, 71 Avenue des Martyrs, CS40220, Grenoble, Cedex 9 38043, France*

[¶]*Department of Chemistry, KULeuven, Celestijnenlaan 200F Box 2404, 3001 Leuven, Belgium*

[§]*CARPOR, Department of Chemical Engineering, University of Liège B6A, Allée du Six Août 13, 4000 Liège, Belgium*

E-mail: cedric.gommes@uliege.be

Abstract

Numerous applications of nanoporous materials require their pores to be filled with liquids. In spite of its huge technological importance, the conditions for the wetting of nanometer-sized pores and its phenomenology are still poorly understood. We report on capillary rise experiments with water in carbon xerogels, with synchrotron small-angle scattering used to follow the process *in situ* at nanometer scale. The data reveal a two-step wetting process whereby water permeates first into molecular-sized micropores, which is followed by the imbibition of the larger mesopores. A Cassie-Baxter analysis shows that the presence of water in the micropores is central as it

turns the mesopores from being hydrophobic to hydrophilic. Based on so-calculated contact angles, the mesopore wetting kinetics are found to be quantitatively described by a classical Washburn model. A modelling of the experimental water profile ahead of the Washburn front reveals strong surface barriers opposing water transfer from the mesopores to the micropres.

Keywords

Nanoscale wetting, Small-angle scattering, Cassie-Baxter states, Microporous materials, Mesoporous materials, Carbon xerogels

Introduction

Countless applications of nanoporous materials require them to be impregnated by liquids. This is the case for many energy conversion and storage technologies,[1–5] adsorption and desalination processes,[6–9] drug-delivery applications,[10] liquid-phase catalysis,[11,12] among others. The impregnation of nanoporous materials by liquids is also central to the preparation of many functional nanomaterials.[13,14] A variety of characterization methods also involve the imbibition of nanometer-sized pores by wetting or non wetting liquids.[15–17] In spite of its huge technological relevance, the wetting of nanoporous materials is a phenomenon that remains poorly understood.

At macroscopic scale, wetting is traditionally discussed in terms of the surface energies of the relevant interfaces, namely : the dry solid, the liquid free surface, and the solid/liquid interface.[18,19] From that perspective, a liquid spontaneously enters a pore whenever the energy of the dry solid is larger than that of the wet solid. This condition is often expressed in dimensionless form by stating that the contact angle between the liquid and solid has to be smaller than 90°. These macroscopic concepts have been successfully used to analyze static and kinetic aspects of porous materials imbibition, with the pioneering

work of Lucas and Washburn[20,21] followed by many others.[22–24] In many instances, however, the complex microstructure of solids and surfaces precludes one from directly applying the general macroscopic concepts.[25–28] A wealth of texture-dependent phenomena are then observed on different surfaces, in relation to contact angle hysteresis,[29] triple-line pinning,[30] super hydro-philicity and -phobicity,[31] precursor wetting phases,[22,32,33] etc. These texture-dependent phenomena are expected to be relevant to the wetting of many porous materials of practical interest, the structure of which is often very disordered with randomly-connected pores having complex shapes over a variety of scales.[23,34–37]

Specific difficulties arise in the context of nanopore wetting. It is usually acknowledged that hydrodynamic models of wetting break down when one approaches the triple line closer than a few tens of nanometers,[38–40] and cutoff lengths have to be introduced to avoid unphysical divergence at small scale. For the materials of interest to us, the latter cutoff lengths are larger than the pores. In addition to the breaking down of macroscopic concepts, specific nanometer-sized phenomena have to be accounted for. They include disjoining pressures and layering effects,[18,41,42] slipping hydrodynamic conditions at surfaces,[43,44] triple-line tension,[45] electrokinetic phenomena,[46,47] capillary condensation,[48] and thermal fluctuations.[49,50] In spite of these general observations, and somewhat surprisingly, some specific macroscopic results pertaining to liquids in pores seem to remain valid down to almost molecular dimensions. This is notably the case for Kelvin's law of capillary condensation,[51] the Navier-Stokes equation itself,[47] and even Young's law.[52] Developing a coherent conceptual framework to analyze and possibly predict the wetting of nanometer-sized pores is still a formidable challenge.

In addition to physical and conceptual difficulties, analyzing wetting at the nanometer-scale is also experimentally challenging. Because of the inherent limitations of electron microscopy, most experimental studies in the field are conducted on model systems such as closed carbon nanotubes or artificial channels, which lack the structural and chemical complexity of porous materials of practical interest.[53–56] In the present work we use synchrotron

small-angle x-ray scattering (SAXS) to analyze *in situ* the nanometer-scale liquid configuration during capillary rise experiments.[57,58] The specific materials we focus on are carbon xerogels,[59–62] which are widely used in catalysis[63] and energy storage applications.[64–66] The structure of carbon xerogels is hierarchical as it comprises molecular-sized micropores coexisting with larger mesopores. The micropores are of particular importance for applications because they contribute most to the specific surface area of the materials, and it is therefore central to ascertain whether and how they are intruded by liquids. The SAXS experiments and data analyses reported in the paper enable one to follow the kinetics of water intrusion into both types of pores.

Experimental Section

Synthesis of the xerogel rods

Xerogels were synthesized through the polycondensation of resorcinol (R) and formaldehyde (F) in water (W), with sodium carbonate (C) to adjust the pH.[67] The specific ratios were the following: an R/F molar ratio of 0.5, a dilution molar ratio W/(R+F+C) of 6, and two different R/C molar ratios of 250 and 350 for X15 and X30. The reacting solutions were poured into test tubes with diameter 5 mm, sealed, and subsequently aged for 72 h at 70°C. The solid gels were then slowly dried inside the opened tubes through the following procedure: 72 h at 70°C at ambient pressure, 24 h at 60°C while progressively decreasing the pressure to 10^3 Pa, 48 h at 70°C and 10^3 Pa, and finally 72 h at 150°C and 10^3 Pa. The dried xerogels are slightly thinner than the initial gels, which enables one to safely remove them from the test tubes.

The so-obtained cylindrical samples were afterwards pyrolized under nitrogen flow to degrade the organic components and leave behind a carbon structure. The pyrolysis involves gradually heating the samples to 800°C at a rate of 2°C/min, with waiting periods at 400°C for 1 h and at 800°C for 2 h, followed by overnight cooling to room temperature. One of the

samples underwent activation to enhance its microporosity. This was done by flowing CO_2 over the sample at 800°C during 8 h.[65,68]

Materials characterization

Nitrogen adsorption and desorption isotherms were measured at -196°C using a Micromeritics ASAP 2420 analyser, following overnight outgassing of the samples at 270°C at pressure below 10^{-2} Pa. The mesopore size d was obtained through a Derjaguin-Brokehoff-de Boer analysis.[69] The nitrogen sorption data were also analyzed using a t-plot,[70,71] in order to discriminate the mesopore and micropore contributions to the pore volume V_m and V_μ, as well as the mesopore surface area A_m.

The meso- and micro-pore volumes are converted to the corresponding volume fractions ϕ_m and ϕ_μ, relative to the total volume of the material (comprising both pore and solid), as follows

$$\phi_{m/\mu} = \frac{V_{m/\mu}}{1/\rho_{\mathrm{c}} + V_m + V_\mu} \tag{1}$$

where $\tilde{\rho}_c$ is the skeletal density of the solid ($\tilde{\rho}_c \simeq 2$ g.cm^{-3} for amorphous carbon). The porosity of the skeleton is then calculated as $\varphi_\mu = \phi_\mu/(1-\phi_m)$. The mesopore surface area A_m (per unit mass) is converted to a_m (per unit volume) as $a_m = A_m\tilde{\rho}_c(1-\phi_m-\phi_\mu)$.

Mercury intrusion porosimetry was measured with ThermoScientific Pascal 140 and 240 porosimeters, operating across a pressure range of 0.01 to 200 MPa corresponding to pores larger than 7.3 nm. When converting intrusion curves to pore sizes, a contact angle of 140° and a surface tension of 0.482 N/m were assumed.[16]

Transmission electron microscopy (TEM) was performed with a Jeol TEM JEM-1400 at 80 kV with a 40,000 magnification. The sample was prepared by crushing it in a mortar into a fine powder, dispersing it in ethanol, and depositing a drop of the supernatant on a microscopy grid.

Water adsorption isotherms were measured at 40°C on the carbon xerogels using a gravi-

metric Dynamic Vapor Sorption (DVS) analyzer from Intrinsic. The data were fitted with the cooperative multi-molecular sorption (CMMS) model,[72] whereby the adsorbed volume of water in micropores is expressed as follows

$$\frac{V}{V_{max}} = \frac{K_0\ P/P_0}{K_0\ P/P_0 + \frac{1}{4}\left[1 - K_1\ P/P_0\sqrt{(1 - K_1\ P/P_0)^2 + 4K_0\ P/P_0}\right]^2} \tag{2}$$

where K_0 and K_1 are two adsorption constants, and $V_{\max}$ is the maximal volume of water that can be adsorbed in the micropores. The volume of water adsorbed at saturation is obtained through Eq. (2) for $P/P_0 = 1$. The values of $V_{\max}$, K_0 and K_1 are reported in the Supporting Information (see Tab. S1).

Synchrotron experiments

Experiments were conducted on the DUBBLE beamline (BM26) at the European Synchrotron Radiation Facility on a setup thoroughly described elsewhere.[73] The energy of the x-rays was adjusted to 12 keV, corresponding to a wavelength of $\lambda = 1.03$ Å. In the used configuration the beam size was 500×500 μm. The SAXS signal was measured on a 2D detector (Pilatus 1M from Dectris with active area 169×179 mm) positioned at 5 m from the sample. The isotropic 2D scattering patterns were converted to 1D scattering curves using the ConeX software,[74] and expressed as $I(q)$ with $q = (4\pi/\lambda)\sin(\theta/2)$ where θ is the scattering angle. The relative position of the sample and detector was calibrated with a silver-behenate reference sample.[75] The experimentally accessible values of q in the setup range from 0.01 to 0.5 Å^{-1}. A photodiode placed on the beamstop was used to measure the transmitted beam intensity I_1, to which all scattering patterns were normalized. An ionization chamber was used to measure the incoming beam intensity I_0.

For the capillary rise experiments, carbon xerogel cylinders were presented in a 3D-printed sample holder with windows on both sides to let the beam through. The holder was wrapped in aluminium foil to avoid water evaporation from the side of the sample during

the experiments (see Fig.1)) A first blank experiment was performed by moving the beam up and down along the cylinder, and measuring the SAXS as well as the incoming and transmitted intensities at 40 intermediate positions over 20 mm with accumulation times of 2 s at each point. The capillary rise experiments then consisted in putting the lower end of the cylinders in contact with a water reservoir and in repeating the same scanning procedure as the blank, over a total duration of 60 min. In practice, the scanning was achieved by keeping the beam in place and moving the experimental stage (sample and water reservoir) up and down with micrometer precision through a stepper motor.

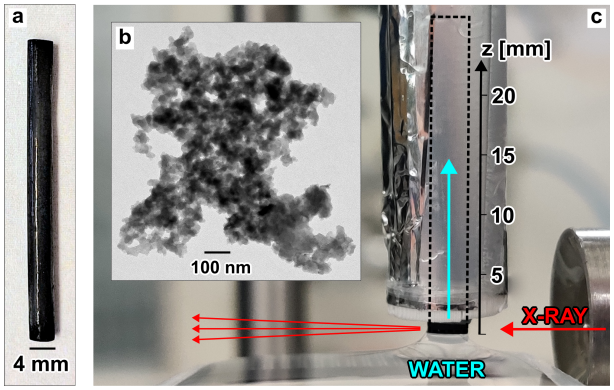

Figure 1: Macroscopic rod of carbon xerogel CX30 (a) and its mesoporous structure as visualized in transmission electron microscopy (b). Capillary rise experiments are initiated by putting the rod in contact with water, and are then followed *in situ* by x-ray absorption and small-angle scattering while scanning the incoming x-ray beam vertically along the rod (c).

The x-ray absorption at any time t and beam position z is estimated from the ratio of the incoming and transmitted intensities as $\alpha \times I_1(z,t)/I_0(t)$. The unknown but constant calibration factor α accounts for the different sensitivity of the photodiode and ionization chamber. Because the absorption results from the presence of carbon and water, Beer-Lambert's relation takes the form

$$\ln\left[I_1(z,t)/I_0(t)\right] + \ln\left[\alpha\right] = -\mu_{\mathrm{c}} l_{\mathrm{c}}(z) - \mu_{\mathrm{w}} l_{\mathrm{w}}(z,t) \tag{3}$$

where $l_w(z,t)$ and $l_c(z)$ are the total lengths of water and carbon crossed by the beam, and

$\mu_{\mathrm{w/c}}$ are the corresponding linear attenuation coefficients. In Eq. (3), the time-dependence of the incoming beam intensity $I_0(t)$ results from the state of the storage ring throughout the experiment, and the space-dependence of the carbon length $l_c(z)$ accounts for the fact that the scanning direction does not necessarily coincide exactly with the axis of the sample. The conditions of the blank experiments are equivalent to setting $l_w = 0$ in Eq.(3), from which one infers the value of $\mu_{\mathrm{c}} l_{\mathrm{c}}(z) + \ln[\alpha]$. The Beer-Lambert law can then be directly inverted to estimate $l_w(z,t)$ during the capillary rise experiments. Throughout the paper, we use the value $\mu_{\mathrm{w}} = 3\ \mathrm{cm}^{-1}$ for the linear attenuation coefficient of water at 12 keV.[76]

In the case of experiments performed on moist samples, dry blank experiments are impossible. In that case the mass uptake measured overnight was converted to a water thickness and added as an offset to the values of $l_w(z,t)$ obtained from Eq. (3).

Results and Discussion

Results

The experiments were performed on macroscopic xerogels, shaped as cylinders with diameter about 4 mm (Fig. 1a). Two xerogel preparations were considered with nominal mesopore sizes 15 and 30 nm, which we refer to as X15 and X30. We comply here with the recommendations of the International Union of Pure and Applied Chemistry (IUPAC) and we refer to pores smaller than 2 nm as *micropores*, and to pores between 2 nm and 50 nm as *mesopores*.[15] The structure of the xerogels consists in a disordered skeleton made up of agglomerated globular objects, with empty spaces corresponding to the mesopores (Fig. 1b). The material that makes up the globules is a dense reticulated polymer with composition similar to phenolic resins.[60,62] Starting from polymer xerogels X15 and X30, carbon xerogels were obtained through pyrolysis. The process converts the polymeric nodules of the skeleton into microporous carbon with turbostratic structure, while minimally affecting the mesopore structure. The obtained materials are referred to as CX15 and CX30. The latter carbon xe-

rogel was further activated in CO_2 to enhance the microporosity of its skeleton,[68,77] leading to sample CX30A.

The two-scale porous structure of carbon xerogels is manifest in the nitrogen sorption isotherms (Fig. 2a), which display both the adsorption-desorption hysteresis typical of mesopores, and the low-pressure steep adsorption typical of microporous materials.[15] Nitrogen sorption in xerogels X15 and X30 display similar adsorption-desorption hysteresis but no micropore adsorption (see Fig. S1). The porous characteristics of the five materials - obtained from nitrogen sorption, mercury intrusion (see Fig. S2) and small-angle scattering - are reported in Tab. 1.

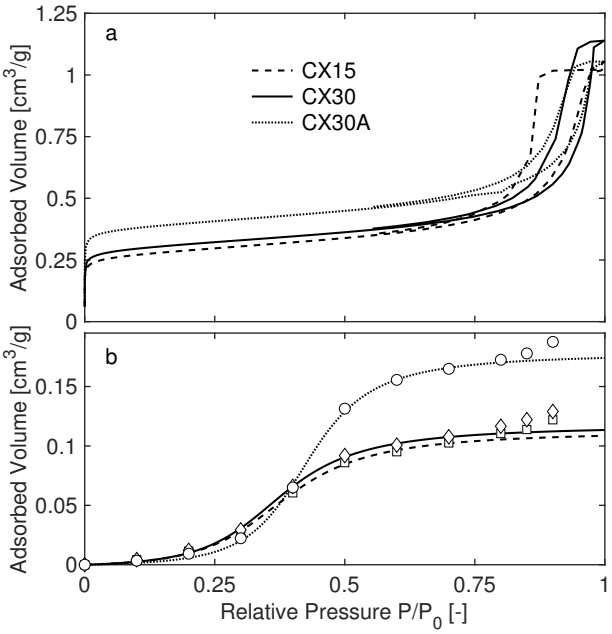

Figure 2: Nitrogen adsorption-desorption isotherms (a) and water sorption isotherms (b) measured on carbon xerogels CX15 (dashed line, □) and CX30 (solid line, ◊), as well as on activated sample CX30A (dotted line, ○). Water sorption isotherms data are fitted with a CMMS model (lines), corresponding to the water content in the micropores (see Eq. 2).

Water sorption isotherms measured on the carbon xerogels (see Fig. 2b) are typical of porous carbons. The adsorption riser around $P/P_0 \simeq 0.4$ corresponds to the filling of the micropores while the mesopores remain largely dry.[78,79] The data were fitted with a cooperative multi-molecular sorption (CMMS) model (lines in Fig. 2b) to determine the volume of water adsorbed in the micropores at saturation. The values reported as $x_\mu^{(sat)}$ in

Tab. 1 show that water fills only about 60 % of the total micropore volume identified by nitrogen sorption.

Table 1: Structural and textural characteristics of the xerogels, derived from nitrogen and water sorption, mercury intrusion, and from small-angle x-ray scattering.

	d [nm]		a_m [$m^2.cm^{-3}$]			ϕ_m [-]	φ_μ [-]	$x_\mu^{(sat)}$ [-]
	N_2	Hg	N_2	Hg	SAXS	N_2	N_2	H_2O/N_2
X15	26	-[a]	108	-[a]	114	0.61	0	-[a]
X30	38	-[a]	83	-[a]	98	0.67	0	-[a]
CX15	18	17	135	122	136	0.53	0.26	0.61
CX30	28	29	115	84	116	0.61	0.28	0.59
CX30A	28	30	119	81	117	0.62	0.36	0.65

d: mesopore diameter; a_m: mesopore surface area; ϕ_m: mesopore volume fraction; φ_μ: pore fraction of the microporous skeleton; $x_\mu^{(sat)}$: fractional water loading of the micropores at saturation.
[a]: not applicable.

The capillary rise experiments were initiated by putting one end of the rods in contact with a deionised water reservoir (Fig. 1c). The synchrotron beam was then repeatedly scanned up and down the rod over a distance of 20 mm, for the entire duration of the capillary rise. X-ray absorption and small-angle scattering data were measured over time at every successive position of the beam. For each carbon xerogel, two experiments were performed. The first was performed on the dry material, *i.e.* after drying the sample overnight at 20 mbar and 150°C to remove water from the micropores. The second experiment was performed on the moist material, after equilibrating the sample overnight in saturated water vapor at room temperature. In the case of non-microporous xerogels X15 and X30, measurements were only done on the dry material.

The x-ray absorption depends on the local quantity of water where the sample is crossed by the beam, and it therefore enables one to follow the capillary rise. Using Beer-Lambert's law, the data is expressed as a space- and time-dependent water length $l_w(z,t)$. This is the cumulated length of water that the synchrotron beam crosses at height z above the bottom

of the rod, at time t after its contact with water. The values measured on all samples are reported in Fig. 3, for the polymer xerogels as well as for the dry and moist carbon xerogels. The non-microporous polymer samples exhibit a sharp wetting front, whereby the amount of water increases to $l_w \simeq 2.4$ mm. The kinetics follows a $t^{1/2}$ Washburn-like scaling, as expected in this context.[21,23,24] Interestingly, in the case of the dry microporous carbon xerogels (Figs. 3b, 3e, 3g) two successive wetting fronts are observed, namely (i) a faint diffuse front where the amount of water increases from zero to about $l_w \simeq 0.2$ mm (from yellow to green in the figure) over a distance z of about 5 mm, followed by (ii) a sharp front whereby the amount of water undergoes a sudden tenfold increase to $l_w \simeq 2.2$ mm (dark blue in the figure).

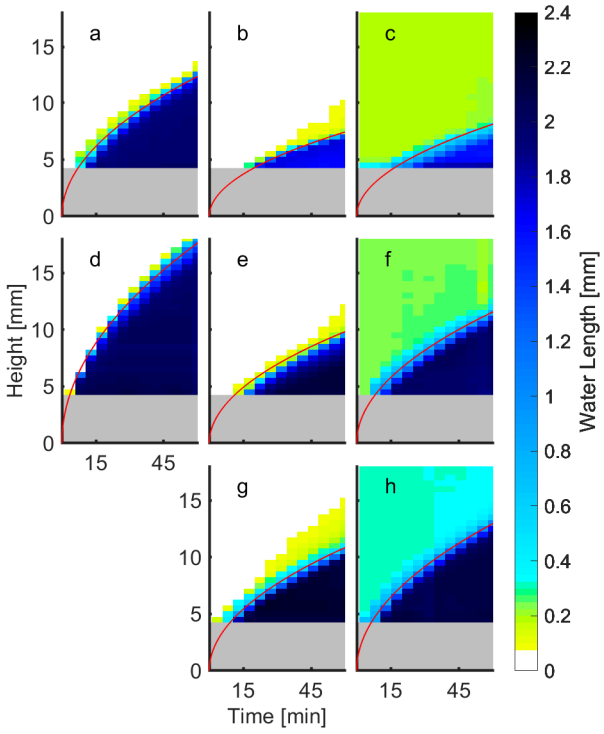

Figure 3: Space- and time-dependent water length $l_w(z,t)$ during capillary rise experiments in polymer xerogels X15 (a) and X30 (d), in dry carbon xerogels CX15 (b), CX30 (e), and in activated carbon xerogel CX30A (g). The rightmost column displays the data for the moist samples: CX15 (c), CX30 (f) and CX30A (h). The horizontal gray area is a blind spot corresponding to the lower part of the sample holder. The red line is a guide to the eye, highlighting a Washburn's $t^{1/2}$ dynamics.

To understand the significance of these two fronts, one has to compare the water thicknesses l_w to the diameter of the carbon rods $L = 4 \pm 0.5$ mm and to the volume fractions reported in Tab. 1. Saturating the micropores with water would correspond to $l_w = L(1-\phi_m)\varphi_\mu x_\mu^{(sat)}$, *i.e.* from 0.25 to 0.4 mm depending on the sample. Saturating the entire porosity would correspond to $l_w = L[\phi_m + (1-\phi_m)\varphi_\mu x_\mu^{(sat)}]$, *i.e.* from 2.3 to 2.7 mm. The sharp front reaching $l_w \simeq 2.2$ mm can therefore safely be assigned to the filling of almost the total pore volume.

Based on x-ray absorption data alone, it is difficult to ascertain the nature of the first diffuse wetting front. It could correspond either to a water film on the outer surface of the skeleton or to the partial filling of the micropores. Based on the skeleton surface area a_m in Tab. 1, one estimates that a water length of 0.2 mm corresponds to a thickness about 4 Å so this would be a very thin film indeed. Moreover, the absence of a diffuse front in the moist samples (Fig. 3c, 3f and 3h) - *i.e.* if the micropores are initially saturated with water - could also be used as an argument in favor of the micropore-filling scenario. A final answer to this question is obtained by considering the small-angle scattering signal.

As a benchmark for the small-angle scattering analysis, Fig. 4 displays the SAXS pattern of dry carbon xerogel CX30A, *i.e.* before the onset of capillary rise. The pattern exhibits the two typical features of materials that are both meso- and micro-porous.[80] The shoulder around $q \simeq 2\ 10^{-2}$ Å^{-1} followed by a q^{-4} Porod scattering is typical of disordered mesoporous structures,[81] and the kink around $q \simeq 2\ 10^{-1}$ Å^{-1} followed by a q^{-2} scattering is typical of the turbostratic structure of microporous carbons.[82,83] The inset displays a realization of a clipped Gaussian field model fitted to the mesopore scattering,[35,84] as well as a qualitative sketch of the small-scale micropore structure. The SAXS patterns of all samples are displayed in the Supporting Information (see Fig. S3).

The relevant contrast to small-angle scattering is the electron density of the various regions of the materials,[57,58] which is modified by the presence of water. Adding water to the micropores would have two distinctly different effects. On one hand it would reduce

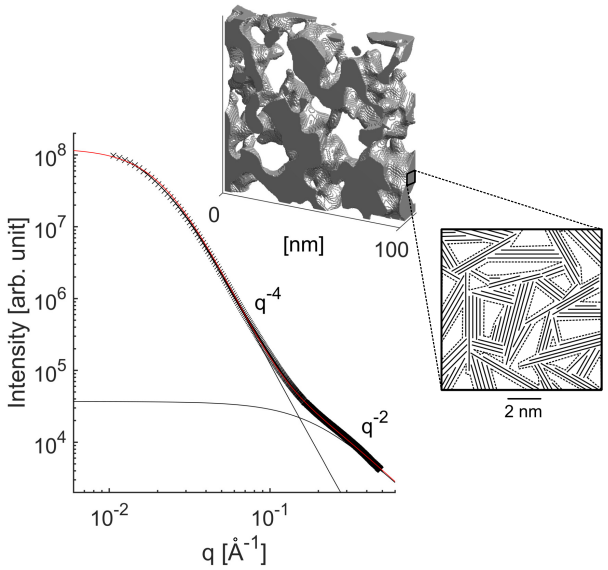

Figure 4: Small-angle x-ray scattering (SAXS) pattern of the dry CX30A sample. The data are shown as crosses; the black lines are fits of the micro- and meso-porous models, and the red line is the sum of both contributions. The inset displays a realization of the clipped Gaussian field model used to fit the mesoporous structure and a sketch of the small-scale structure of the microporous skeleton.

the scattering contrast between the micropores and the neighbouring dense carbon in the skeleton, thereby weakening micropore scattering (at high q). On the other hand, it would increase the average electron density of the microporous skeleton as a whole, thereby enhancing the mesopore scattering (at low q). Filling the mesopores with water would simply reduce the contrast between the mesopores and the microporous skeleton, and lower the mesopore scattering.

During our experiments, SAXS was measured continuously during capillary rise, *i.e.* one full pattern similar to Fig. 4 was recorded for every position and time shown in Fig. 3. A small selection of this large dataset is displayed in Fig. 5, corresponding to a z-scan across the two successive wetting fronts in CX30A (from $z = 8$ mm to $z = 14$ mm, around $t = 60$ min). For clarity, the absorption data (same as in Fig. 3) is displayed in the inset of Fig. 5a, with the same color code as in the rest of the figure. Interestingly, the diffuse wetting front (from dark red to green) is accompanied by both a decrease of the SAXS at high q (Fig. 5c) and an increase at low q (Fig. 5b). This was the anticipated evolution for the

filling of micropores. The sharp wetting front (from orange to bright blue) is found to be accompanied by a tenfold decrease of the SAXS intensity at all q (Fig. 5a), as was expected for the filling of the mesopores.

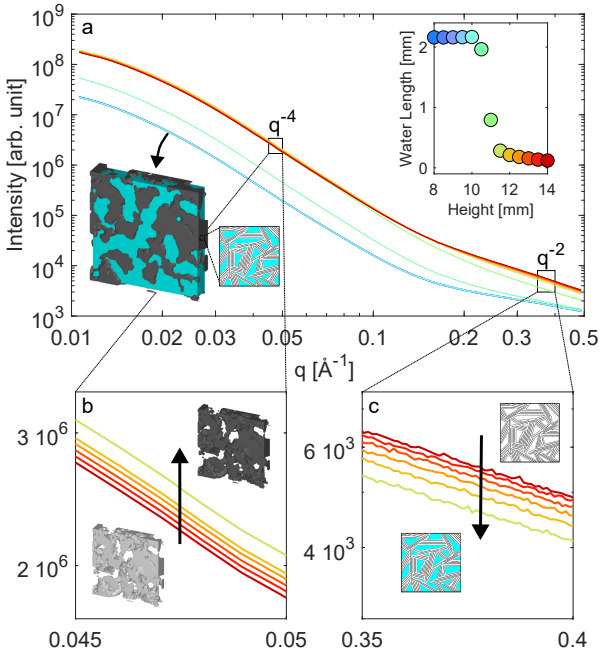

Figure 5: Example of SAXS patterns measured in CX30A at different heights z across the wetting front (a), with the inset indicating the quantity of water at each height and specifying the relation between the color and z. Magnified view of the SAXS testify to opposite evolutions of the SAXS at low and high values of q (b and c). The sketches illustrate the water filling corresponding to the observed SAXS evolution.

To make these observations quantitative, the SAXS data in the crossover region between meso- and micropore scattering (*i.e.* above $q \simeq 0.05$ Å^{-1}) was fitted with the following equation[82]

$$I(q) = Aq^{-4} + B\frac{l^2(18 + (ql)^2)}{(9 + (ql)^2)^2} \tag{4}$$

where parameters A and B capture and discriminate the scattering contributions of the meso- and micro-pores, respectively. In Eq. (4), the first term accounts for the Porod scattering of the mesopore surface and the second term accounts for the micropore scattering, with size parameter l scaling with the micropore size.[85] Figure 6 displays the so-obtained values of

A and B for every available position and time during capillary rise experiments in all the dry carbon xerogels, plotted against the corresponding total length of water $l_w(z,t)$. The values are normalized to their initial value, A_{dry} and B_{dry}. The vertical lines in the figure are the lengths of water corresponding to saturated micropores, based on the values of $x_\mu^{(sat)}$ from water adsorption (Tab. 1). The equivalent data for non-microporous polymer xerogels X15 and X30, as well as for the initially moist carbon xerogels are shown in the Supporting Information (see Figs. S4 and S5).

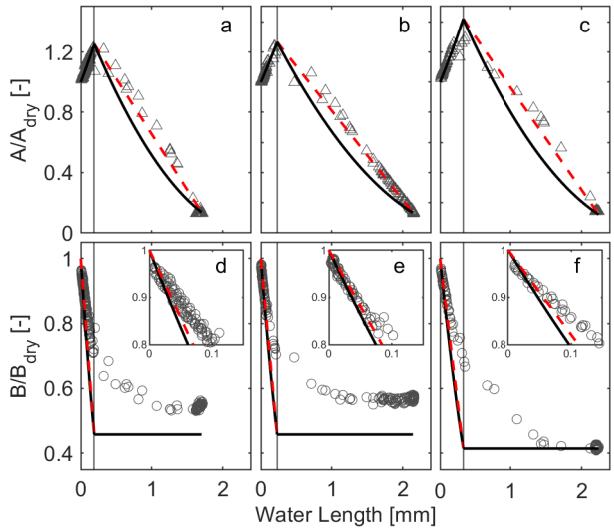

Figure 6: Mesopore (top row) and micropore (bottom row) scattering during capillary rise experiments in dry carbon xerogels CX15 (a, d), CX30 (b, e) and CX30A (c, f). The vertical lines correspond to the equilibrium filling of the micropores. Solid black lines are calculated for the progressive filling of micropores, followed by that of mesopores. For the dashed red lines, the progressive filling of pores is replaced by coexisting empty and filled pores with increasing proportions (see text).

The scenario whereby the micropores fill first and the mesopores afterwards, can be quantitatively tested against the values of the scattering intensities A and B, based on the electron densities of carbon and water ($\rho_c \simeq 0.6$ e$^-$/Å^3 and $\rho_w \simeq 0.33$ e$^-$/Å^3) and on the volume fractions in Tab. 1. In the case of pure micropore filling (*i.e.* with no water in the mesopores), the fractional water loading of the micropores is calculated as l_w/l_μ, where l_μ is the total micropore length, estimated as $L(1-\phi_m)\varphi_\mu$ where L is the sample thickness.

Therefore, the average electron density in the micropores is

$$\rho_\mu(l_w) = \rho_w \times (l_w/l_\mu) \tag{5}$$

where l_w/l_μ takes values from 0 to $x_\mu^{(sat)}$. The corresponding micropore scattering is proportional to $B \propto [\rho_\mu - \rho_c]^2$ where the factor is irrelevant when normalizing by the dry value B_{dry}. Over the same range of l_w, the average electron density of the microporous skeleton as a whole is calculated as

$$\rho_s(l_w) = \rho_c(1 - \varphi_\mu) + \rho_w\varphi_\mu \times (l_w/l_\mu) \tag{6}$$

The mesopore scattering is then calculated as $A \propto [\rho_s]^2$, because the relevant contrast is between the skeleton and the empty mesopore. The so-calculated values of A and B are plotted as solid black lines in Fig. 6 for values of l_w from 0 to micropore saturation $l_\mu x_\mu^{(sat)}$.

When l_w exceeds the micropore saturation, the filling of the micropores remains constants and so does the scattering B. The value of l_w in excess of $l_\mu x_\mu^{(sat)}$, however, contributes to filling the mesopores and increase its electron density as

$$\rho_m(l_w) = \rho_w \times (l_w - l_\mu x_\mu^{(sat)})/l_m \tag{7}$$

where l_m is the total mesopore length. The mesopore scattering is then calculated as $A \propto [\rho_m(l_w) - \rho_s(l_\mu x_\mu^{(sat)})]^2$. The so-obtained values of A and B for l_w larger than $l_\mu x_\mu^{(sat)}$ are plotted in Fig. 6.

For completeness, the possibility of heterogeneous filling of both micro- and meso-pores was also considered. In that scenario, pores can be either empty or saturated; the progressive and homogeneous filling is replaced by increasing the proportion of saturated pores. With this scenario, the scattering is calculated as linear interpolation of the initial and end states. This is shown as dashed red lines in Fig. 6.

These simple considerations quantitatively capture the mesopore scattering, during the imbibition of both micropores and mesopores (Fig. 6a to 6c). The same holds for the polymer xerogels and the initially moist carbon xerogels (see Figs. S4 and S5 in the Supporting Information). Some aspects of the high-q scattering in Figs. 6d to 6f, however, are not accounted for. In particular, the decrease of B is more progressive than in the simple scenario and its final value is slightly underestimated in the non-activated samples CX15 and CX30 (Fig. 6d and 6e). A variety of phenomena could explain these differences. The micropores might not be saturated yet at the arrival of the mesopore wetting front, and they would fill up in direct contact with water. Also, should the filling of the mesopores happen through the thickening of a wetting film on the wall, this would lead to an additional q^{-2} scattering[86] that would be difficult to discriminate from the micropore scattering in Eq. (4). To put these considerations under perspective, however, one has to keep in mind that mesopore imbibition is overrepresented in Fig. 6, which condenses in a single plot the SAXS data measured at all heights and all times. In reality, mesopore filling is a fast process that is barely resolved experimentally, as visible in the inset of Fig. 5a.

Discussion

The in-situ scattering data during capillary rise experiments reveal a two-step wetting mechanism of carbon xerogels, whereby water imbibes first molecular-sized micropores before invading the mesopores. This raises two main questions about how the presence of water in the micropores modifies the wetting of the mesopores, and about physical processes driving water into the micropores.

To discuss these points, consider Fig. 7, which illustrates the time-dependent water profile in the micropores across the wetting front, based on two qualitatively different physical measurements. In Fig. 7a$_1$, the fractional water loading of the micropores x_μ is estimated from the high-q small-angle scattering B/B_{dry} through the water-dependent contrast between the micropore electron density and dense carbon (see Eq. 5). The value of x_μ saturates at

$x_\mu^{(sat)}$ after the mesopore wetting front. In Fig. 7a$_2$, the micropore filling is estimated from absorption as l_w/l_μ, where l_w and l_μ are the total length of water and of micropores on the x-ray path. The values in excess of 1 are due to water in the mesopores. From these profiles, the position of the mesopore wetting front was determined as the center of the steep riser ($l_w/l_\mu \simeq 0.4$). The position of the micropore front is not uniquely defined because of its diffuse nature. The values reported in Figs. 7b are calculated from the integrated volume of water in the micropores, and expressed as an equivalent thickness of water-saturated microporous skeleton (see green line in Fig. 7a$_1$). The data follow a kinetics of the type $z^2 = Dt$, and we refer to the slopes of the meso- and micro-pore wetting fronts as D_m and D_μ. The corresponding figures for polymer xerogels CX15 and CX30 are in the Supporting Information (see Fig. S6) as well as the values of the Washburn coefficients D_m and D_μ for all samples (see Tab. S2).

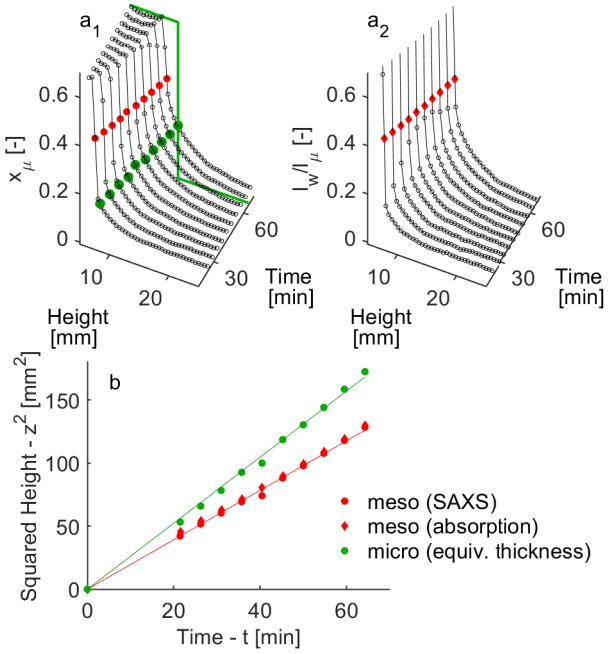

Figure 7: Water content of the micropores ahead of the mesopore wetting front, as seen from SAXS (a$_1$) and from x-ray absorption (a$_2$) in carbon xerogel CX30A. The mesopore front (red) and the equivalent height of the saturated micropores (green) follow a Washburn dynamic with constant slope $D = z^2/t$ (b).

The distinctive $t^{1/2}$ kinetics observed in Fig. 7b hints at a Washburn mechanism,[21–23]

whereby the negative capillary pressure pulling water into the pores is constant, but the viscous resistance increases proportionally to the height of the water column. In the case of a xerogel that is initially dry, some of the water rising in the mesopores is diverted towards the micropores. We show in the Supporting Information (Sec. S3) that such a scenario leads to the following Washburn coefficient for the mesopore wetting

$$D_m = \frac{8K_m}{\eta[\phi_m + (1-\phi_m)\varphi_\mu x_\mu^{(sat)}]} \times \frac{\gamma_w \cos(\theta)}{d} \tag{8}$$

where K_m is the hydraulic permeability of the xerogel, η is the viscosity of water, d is the mesopore size, γ_w is the surface tension of water, and θ is the equilibrium contact angle between mesopore water and the skeleton. The volume fractions ϕ_m and φ_μ in the denominator account for the volume of the pores that are progressively filled during capillary rise. In the case of moist xerogels with micropores initially saturated, the relevant value is $\varphi_\mu = 0$ independently of the actual microporosity. Equation (8) can be used to infer the values of the contact angle from the wetting kinetics, provided the permeability is known. We rely here on the Kozeny-Carman relation

$$K_m = \frac{\phi_m^3}{C a_m^2} \tag{9}$$

where a_m is specific surface area of the mesopores and C is an empirical constant close to 5 in disordered porous solids.[87–89] The values of the contact angle inferred from the mesopore wetting kinetics are plotted in Fig. 8. The error bars result from assuming $C = 2.5$ and $C = 10$ as conservative lower and upper bounds for the Kozeny-Carman constant.[90,91] The mesopore surface areas used for the calculation are those inferred from SAXS, and the pore sizes are those from nitrogen sorption (see Tab. 1).

The contact angles estimated for the polymer xerogels X15 and X30 are around $67 \pm 1°$, which is very close to the 70° macroscopic contact angle of water on non-porous phenolic resin coatings.[92] In the case of the carbon xerogels, all the calculated contact angles are

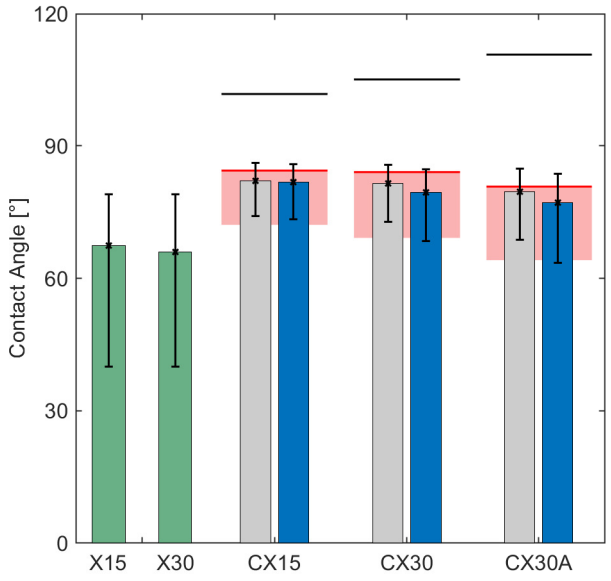

Figure 8: Contact angles calculated from the wetting of the mesopores in polymer xerogels (green), as well as in the initially dry (grey) and moist (blue) carbon xerogels, with error bars resulting from the uncertainty on the Kozeny-Carman constant C. The horizontal black lines and red bands are Cassie-Baxter estimations of the contact angles in the dry and moist carbon xerogels. The vertical breadth of the red bands results from assuming saturated ($x_\mu^{(sat)}$ in Tab. 1) or water-filled ($x_\mu = 1$) micropores.

gathered around $80 \pm 2°$ in spite of the Washburn constants D_m differing by more than a factor two among all considered samples (see Tab. S2). Interestingly, this applies both to initially dry and moist carbon xerogels. In other words, the reason why the mesopore wetting in the dry carbon xerogels is slower is that some water rising in the mesopores is diverted into the micropores. The very driving force of the process, *i.e.* the capillary pressure or the contact angle in the mesopores, is therefore identical irrespective of whether the micropores are initially dry or saturated. This clearly points to the presence of water in the micropores, before the arrival of the mesopore wetting front.

Although the contact angle θ has no geometrical significance in the present nanometer-scale context, there is evidence that it still has physical relevance at that scale.[51,52] In that respect, the physically meaningful quantity in Eq. (8) is the product $\gamma_w \cos(\theta)$, which is numerically equal to the energy difference between the wet and dry solid through the Young-Dupré relation.[18] From that perspective, the contact angle is merely a measure of

a surface energy difference, expressed in dimensionless form through normalization by the surface tension of water γ_w.

The surface energies relevant to mesopore wetting are those of the microporous skeleton, in contact with either air or water. The microporous skeleton, however, comprises three distinct phases: the carbon, the water-filled fraction of the micropores, and the empty fraction of the micropores. Following a Cassie-Baxter approach[93,94] one may assume additive contributions of the three phases to the surface energy, namely

$$\cos(\theta) = (1 - \varphi_\mu)\cos(\theta_c) + x_\mu\varphi_\mu - (1 - x_\mu)\varphi_\mu \tag{10}$$

In this equation, the first term accounts for the interaction of the mesopore water with carbon (contact angle $\theta_c \simeq 86°$, assuming graphite[95,96]), the second with the micropore water (corresponding to $\cos(\theta) = +1$) and the third with the empty micropores (corresponding to $\cos(\theta) = -1$).

The contact angle relevant to the hypothetical wetting of the dry skeleton (with no water in the micropores) corresponds to setting $x_\mu = 0$ in Eq. (10). The so-calculated contact angles are shown as black lines in Fig. 8. The values being larger than 90°, it would not be energetically favourable for water to enter the mesopores at all, if the micropores were dry. By contrast, the contact angles calculated assuming water in the micropores, are all smaller than 90° and close to the values inferred from the wetting kinetics. In Fig. 8, the solid red line is the contact angle calculated for each sample from the Cassie-Baxter approach in Eq. (10) with water filling corresponding to $x_\mu^{(sat)}$. The thicker red area extends over all intermediate micropore filling from $x_\mu^{(sat)}$ to $x_\mu = 1$.

Because the presence of water in the micropores is key to the wetting of the mesopores, one has to enquire about the mechanism that drives water into the micropores ahead of the mesopore wetting front. The existence of such precursors of impregnation is common on textured surfaces.[28,33,39] In the present context, a Washburn wetting mechanism in the

microporous skeleton would lead to micropore wetting kinetics of the type $H_\mu = \sqrt{D_\mu t}$, in qualitative agreement with Fig. 7b.[22] Quantitatively, however, the micropore permeability needed to account for the experimental values of D_μ is of the order of 0.5 Å^2 (see Supporting Information Sec. S3), which is unrealistically small. Moreover, the diffuse nature of the micropore wetting front can hardly be accounted for by a classical Washburn scenario. We therefore explore the possibility of water diffusion in the mesopores accompanied by its adsorption into the microporous skeleton.

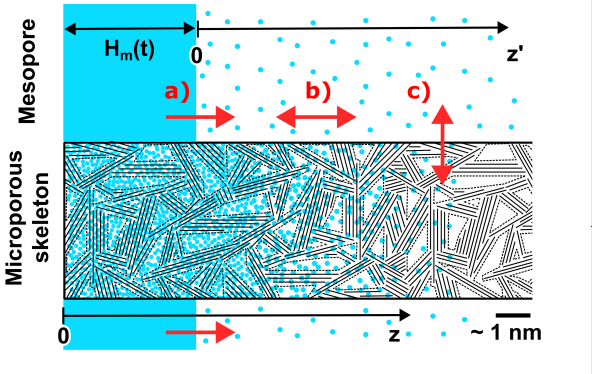

Figure 9: Sketch of the diffusion-adsorption model for analyzing the water profile ahead of the mesopore wetting front, involving the movement of the mesopore wetting front (a), the diffusion of the water in the mesopores (b) and its adsorption into the microporous skeleton (c). The static and moving coordinates are defined as z and $z' = z - H_m(t)$.

More specifically, the process we consider is a competition between the diffusion of water molecules in the mesopores and the movement of the Washburn wetting front from which they originate, which constantly catches up with them. The process is sketched in Fig. 9. We introduce the moving coordinates $z' = z - H_m(t)$, such that the mesopore wetting front is constantly at position $z' = 0$. The actual form of the mobile water molecules ahead of the Washburn front is unclear yet, and we assume for now that they are in the vapor phase. In that spirit, we quantify the water concentration through the relative humidity $x_m(z', t)$ and model its transport with the following convection-diffusion-adsorption equation in the z' coordinates

$$\frac{\partial x_m}{\partial t} = \left(\frac{dH_m}{dt}\right)\frac{\partial x_m}{\partial z'} + D\frac{\partial^2 x_m}{\partial z'^2} - k\left\{x_m - x_m^{(eq)}[x_\mu]\right\} \tag{11}$$

where the first term on the right-hand side accounts for upward movement of the reference frame, the second term accounts for water diffusion, and the last term accounts for the local water transfer between the mesopores and the microporous skeleton. That term is modelled here as a first-order law with kinetic constant k, and $x_m^{(eq)}[x_\mu]$ is the equilibrium relative humidity in the mesopore corresponding to micropore filling x_μ. In the present case of carbon xerogels, the equilibrium adsorption function $x_m^{(eq)}[x_\mu]$ is well described by the CMMS model (see Eq. 2). As boundary conditions, we impose that the vapor is saturated on the wetting front ($x_m = 1$ at $z' = 0$) and that the material is dry far from it ($x_m = 0$ for $z \to \infty$). In order to close Eq. (11), a conservation law has to be written also for the micropore filling fraction, which is the following

$$\frac{\partial x_\mu}{\partial t} = \left(\frac{dH_m}{dt}\right) \frac{\partial x_\mu}{\partial z'} + ak \left\{x_m - x_m^{(eq)}[x_\mu]\right\} \tag{12}$$

where we have neglected a diffusion term, because diffusion in micropores is orders of magnitude slower than in mesopores.[97] The last term in Eq. (12) is identical to Eq. (11) except for the sign and for the dimensionless constant

$$a = \frac{C_0 v_0 \phi_m}{\phi_\mu} \tag{13}$$

where C_0 is the saturated vapor concentration at the considered temperature, v_0 is the molecular volume of water in the micropores, and ϕ_m (ϕ_μ) is the mesopore (micropore) volume fraction. It has to be stressed that Eqs. (11) and (12) also apply if the mobile water molecules are not in the vapor phase. In that more general setting, parameter a is the number ratio of molecules in the mobile and adsorbed states. Because x-ray data show that almost all water molecules ahead of the wetting front are in the micropores (compare Figs. 7a$_1$ and 7a$_2$) the value of a has to be very small. The value inferred from Eq. (13) and the characterization data in Tab. 1 is around $a \simeq 1.5\ 10^{-4}$.

The numerical method used to solve Eqs. (11) and (12) is described in Sec. S4 of the

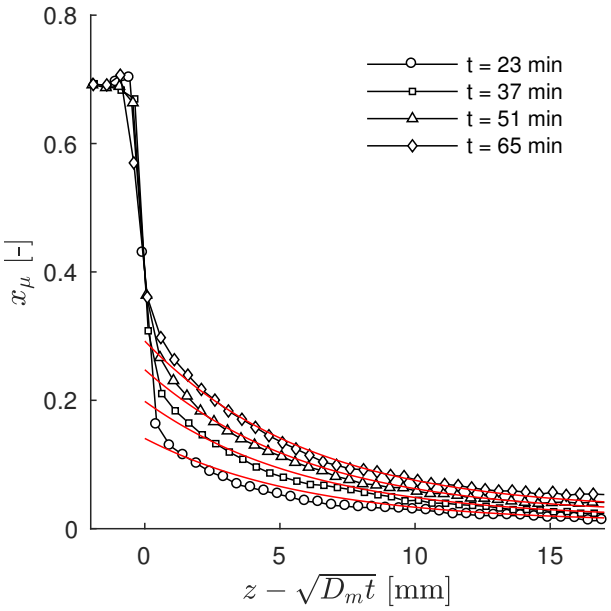

Figure 10: Space- and time-dependent fractional water loading of the micropores $x_\mu(z,t)$ in front of the mesopore wetting front in CX30A (same data as in Fig. 7) with the calculated values from the diffusion-adsorption model with $D \simeq 8.8\ 10^{-5}$ m^2.s^{-1} and $k = 2.7$ s^{-1} (red lines).

Supporting Information, together with additional mathematical details. Figure 10 shows that the space- and time-dependent fractional water loading of the micropores $x_\mu(z',t)$ in CX30A is well captured by the diffusion-adsorption model. The same holds for the other two carbon xerogels considered in this work (see Supporting Information, Fig. S7). It is useful to stress that although the mobile water is assumed to be saturated at the mesopore wetting front ($x_m = 1$ at $z' = 0$), the actual micropore filling x_μ results from a competition between diffusion, adsorption, and the movement of the wetting front. Using a quasi-static approximation of Eqs. (11) and (12), these effects are shown in the Supporting Information to be captured by dimensionless number

$$\frac{1}{Dka^2}\left(\frac{dH_m}{dt}\right)^2 \tag{14}$$

which effectively compares the mesopore wetting speed dH_m/dt to the characteristic velocity $a\sqrt{Dk}$ (see Fig. S10). Accordingly, the experimentally observed increase of the micropore

filling $x_\mu(0)$ in Fig. 10 is attributed to the progressive slowing down of the mesopore wetting front. For all samples, the model parameters inferred by least-square fitting of the data are $D \simeq 1.3 \pm 0.5\ 10^{-4}$ m^2.s^{-1} and $k \simeq 2 \pm 0.6$ s^{-1}. The corresponding characteristic velocity is around $a\sqrt{Dk} \simeq 2.5\ 10^{-6}$ m.s^{-1}, which compares with the 0.1 mm.min^{-1} velocity of the Washburn front.

To gain physical insight from the values of k and D, we first estimate the time needed for water molecules to diffuse inside the micropores over the thickness l_s of the skeleton. Assuming conservative values $l_s \simeq 10$ nm and $D_\mu \simeq 10^{-13}$ m^2.s^{-1} for the diffusion coefficient in micropores,[97] the diffusion time is $l_s^2/D_\mu \simeq 10^{-3}$s. Because this is three orders of magnitude faster than the observed time $1/k \simeq 1s$, one can safely conclude that adsorption is not limited by micropore diffusion. As an alternative, adsorption into microporous solids is often limited by surface resistance,[98,99] as a consequence of either micropore constriction close to the surface[100] or of the reduced degrees of freedom of adsorbed molecules.[101] To analyze this, it is useful to consider that the last term in Eq. (11) is the difference between an adsorption and a desorption fluxes, kx_m and $kx_m^{(eq)}(x_\mu)$ respectively, which enables one to use kinetic theory of gases to express the kinetic constant as[98]

$$k = \epsilon \times \sqrt{\frac{k_B T}{2\pi m}} \times \frac{a_m}{\phi_m} \tag{15}$$

where the square root is the surface collision frequency for unit area and unit concentration of gas,[102] with m being the molecular mass of water, a_m/ϕ_m is the surface-to-volume ratio of the mesopores, and ϵ is the fraction of water molecules hitting the mesoporous surface that actually enter the micropores. The latter parameter characterizes surface resistance. Based on the surface areas in Tab. 1, the experimental values of k point at extremely low values of the order of $\epsilon \simeq 10^{-10}$. We are not aware of independent measurements of ϵ for microporous carbon, but the present value is four orders of magnitude smaller than that observed in zeolites.[98] Values as small as $\epsilon \simeq 10^{-15}$ have been discussed theoretically.[101]

Concerning the diffusion coefficient D, a first observation is that its experimental value is orders of magnitude larger than the typical diffusion coefficient in micropores D_μ. This confirms that micropore diffusion does not contribute to the overall water transport, as is implicit in Eq. (12). In case water transport would take place in the vapor phase, the expected diffusion coefficient would compare with the Knudsen value[103]

$$D_K = \frac{d}{3}\sqrt{\frac{8k_BT}{\pi m}} \times \frac{\phi_m}{\tau} \tag{16}$$

where d is the mesopore size and τ is a tortuosity factor that is often approximated as $\tau \simeq 1/\phi_m$. Based on the pore sizes in Tab. 1 the Knudsen diffusion coefficient is close to $D_K \simeq 1.7\ 10^{-6}$ m^2.s^{-1}. Because the experimental values are two orders of magnitude larger, vapor-phase diffusion has to be ruled out too. Based on the available data, one can only speculate on the underlying transport mechanism. From the general observation that the mobile species are a small fraction of all the water molecules, a molecular-thin film on the mesopore surface would be a plausible assumption. Such a thin film would contribute to a weak q^{-2} SAXS signal, which could explain some of the deviations from the exclusive micropore-filling scenario in Fig. 6d-f. Concerning the transport coefficients, one should stress that - unlike Knudsen diffusion - there are energy incentives to the spreading of water molecules on a carbon surface.[104] When phenomenologically describing such energy-driven phenomenon as a passive diffusion process, large apparent diffusion coefficients are indeed expected. Exploring these questions in detail would, however, require different type of experiments and is outside the scope of the present paper.

Conclusions

The wetting of carbon xerogels occurs through two successive steps: water permeates first the molecular sized micropores and this is followed by the imbibition of larger mesopores. In the context of capillary rise experiments, these two steps are evidenced as two successive

wetting fronts. The presence of water in the micro- or meso-pores has distinctly different effects on the small-angle scattering signal, which enables one to discriminate the two wetting processes. Knowing that wetting is such a two-step process provides one with conceptual tools to quantitatively understand it.

All data concerning the wetting of the mesopores, down to 15 nm in size, are here found to be well described by classical concepts from macroscopic physics. The contact angle between the mesopore water and the microporous skeleton seem to follow a Cassie-Baxter mechanism, in particular when the micropores are permeated with water. And the mesopore wetting kinetics quantitatively follows Washburn's law, assuming a Kozeny-Carman permeability with classical values for the parameters. The usefulness of a Cassie-Baxter approach at nanometer scale is not surprising, because it merely expresses the additive contribution of all constituents of the dry or wet microporous skeleton to the dispersive forces experienced by water in the mesopores. The observation of Washburn kinetics in this context is not novel,[23] and it is also in line with the known accuracy of hydrodynamics down to the nanometer scale.[40] However, the accuracy of predictions based on macroscopic surface energies and contact angles is perhaps surprising.

Concerning triple-line tension, it was not expected to play a role as a driving force in the present context. When the menisci in the mesopores move upwards by a macroscopic distance, the triple-line is shifted up but its length remains unchanged. This is energetically neutral. However, because of the disordered structure of the xerogels, any microscopic displacement of the menisci is necessarily accompanied by triple-line length fluctuations. In principle, the latter fluctuations could contribute to energy dissipation, and therefore to slowing down the wetting. If this effect is present, it is within the error bars of our data. Most energy dissipation seems to result from bulk viscous effects. This is not something one would necessarily presume, if one were to extrapolate to nanometer-scale results from macroscopic wetting.[28]

Interestingly, the presence of water in the micropores is found to be key for the wetting

of the larger mesopores. The permeation of water into the micropores does not follow a Washburn scenario. Based on the diffuse shape of the water profiles, we hypothesised a general mechanism whereby a small fraction of water diffuses in the mesopores ahead of the main wetting front, and is then captured by the microporous skeleton. To account for the experimental water profiles, the model has to invoke a large mobility of water molecules in the mesopores (about hundred times larger than Knudsen diffusion) which leaves the question of the exact transport mechanism unanswered. Interestingly, the analysis also points at strong kinetic barriers opposing the entrance of water molecules into the micropores. Similar barriers have been reported for gas adsorption by other types of microporous solids. Their observation and relevance in the present context opens new prospects for controlling the wettability of nanoporous carbons.

Acknowledgement

C.J. Gommes is grateful to the Funds for Scientific Research (F.R.S.-FNRS, Belgium) for a research associate position and for supporting this research through grant PDR T.0100.22. A. F. Léonard thanks the University of Liège (Fonds Spéciaux pour la Recherche FSR) and the Fonds de Bay for their financial supports.

Supporting Information Available

Additional characterization data of the porous samples, and mathematical/numerical procedures. All data are available for downloading from the authors' institutional data repository (10.58119/ULG/4WAKO6). This material is available free of charge via the Internet at `http://pubs.acs.org/`.

References

1. Frackowiak, E.; Béguin, F. Carbon Materials for the Electrochemical Storage of Energy in Capacitors. *Carbon* **2001**, *39*, 937–950.

2. Ghosh, S.; An, X.; Shah, R.; Rawat, D.; Dave, B.; Kar, S.; Talapatra, S. Effect of 1- Pyrene Carboxylic-Acid Functionalization of Graphene on its Capacitive Energy Storage. *J. Phys. Chem. C* **2012**, *116*, 20688–20693.

3. Kado, Y.; Soneda, Y.; Hatori, H.; Kodama, M. Advanced Carbon Electrode for Electrochemical Capacitors. *Solid-State Electron.* **2019**, *23*, 1061–1081.

4. Xu, W.; Lu, Z.; Sun, X.; Jiang, L.; Duan, X. Superwetting Electrodes for Gas-Involving Electrocatalysis. *Acc. Chem. Res.* **2018**, *51*, 1590–1598.

5. Deshpande, R. A.; Navne, J.; Adelmark, M. V.; Shkondin, E.; Crovetto, A.; Hansen, O.;

Bachmann, J.; Taboryski, R. Understanding the Light Induced Hydrophilicity of Metal-Oxide Thin Films. *Nat. Commun.* **2024**, *15*, art. no. 124.

6. Yu, F.; Li, Y.; Han, S.; Ma, J. Adsorptive Removal of Antibiotics from Aqueous Solution Using Carbon Materials. *Chemosphere* **2016**, *153*, 365–385.

7. Pillai, A.; Kandasubramanian, B. Carbon Xerogels for Effluent Treatment. *J. Chem. Eng. Data* **2020**, *65*, 2255–2270.

8. Medina, O. E.; Galeano-Caro, D.; Castelo-Quibén, J.; Ocampo-Peez, R.; Pérez-Cadenas, A. F.; Carrasco-Marín, F.; Franco, C. A.; Corteś, F. B. Monolithic Carbon Xerogels-Metal Composites for Crude Oil Removal from Oil in-Saltwater Emulsions and Subsequent Regeneration Through Oxidation Process: Composites Synthesis, Adsorption Studies, and Oil Decomposition Experiments. *Microporous Mesoporous Mater.* **2021**, *319*, art. no. 111039.

9. Porada, S.; Zhao, R.; Van Der Wal, A.; Presser, V.; Biesheuvel, P. Review on the Science and Technology of Water Desalination by Capacitive Deionization. *Prog. Mater. Sci.* **2013**, *58*, 1388–1442.

10. Vallet-Regi, M.; Balas, F.; Arcos, D. Mesoporous Materials for Drug Delivery. *Angew. Chem., Int. Ed.* **2007**, *46*, 7548–7558.

11. Job, N.; Marie, J.; Lambert, S.; Berthon-Fabry, S.; Achard, P. Carbon Xerogels as Catalyst Supports for PEM Fuel Cell Cathode. *Energy Convers. Manage.* **2008**, *49*, 2461–2470.

12. Bailón-García, E.; Drwal, E.; Grzybek, T.; Henriques, C.; Ribeiro, M. F. Catalysts Based on Carbon Xerogels with High Catalytic Activity for the Reduction of NOx at Low Temperatures. *Catal. Today* **2020**, *356*, 301–311.

13. De Jongh, P. E.; Eggenhuisen, T. M. Melt Infiltration: An Emerging Technique for the Preparation of Novel Functional Nanostructured Materials. *Adv. Mater.* **2013**, *25*, 6672–6690.

14. Munnik, P.; De Jongh, P. E.; De Jong, K. P. Recent Developments in the Synthesis of Supported Catalysts. *Chem. Rev.* **2015**, *115*, 6687–6718.

15. Rouquerol, J.; Avnir, D.; Fairbridge, C. W.; Everett, D. H.; Haynes, J. H.; Pernicone, N.; Ramsay, J. D. F.; Sing, K. S. W.; Unger, K. K. Recommendations for the Characterization of Porous Solids. *Pure Appl. Chem.* **1994**, *66*, 1739–1758.

16. Giesche, H. Mercury porosimetry: A general (practical) overview. *Part. Part. Syst. Charact.* **2006**, *23*, 9–19.

17. Petrov, O. V.; Furó, I. NMR Cryoporometry: Principles, Applications and Potential. *Prog. Nucl. Magn. Reson. Spectrosc.* **2009**, *54*, 97–122.

18. de Gennes, P. G.; Brochard-Wyart, F.; Quéré, D. *Capillarity and Wetting Phenomena*; Springer: New York, 2003.

19. Yuan, Y.; Lee, T. R. *Contact Angle and Wetting Properties*; Springer, 2013; Vol. 51.

20. Lucas, R. Ueber das Zeitgesetz des Kapillaren Aufstiegs von Flossigkeiten. *Kolloid-Z.* **1918**, *23*, 15–22.

21. Washburn, E. W. The Dynamics of Capillary Flow. *Phys. Rev.* **1921**, *17*, 273–283.

22. Bico, J.; Quéré, D. Precursors of Impregnation. *Europhys. Lett.* **2003**, *61*, 348–353.

23. Gruener, S.; Sadjadi, Z.; Hermes, H. E.; Kityk, A. V.; Knorr, K.; Egelhaaf, S. U.; Rieger, H.; Huber, P. Anomalous Front Broadening During Spontaneous Imbibition in a Matrix with Elongated Pores. *Proc. Natl. Acad. Sci. U. S. A.* **2012**, *109*, 10245–10250.

24. Cai, J.; Jin, T.; Kou, J.; Zou, S.; Xiao, J.; Meng, Q. Lucas-Washburn Equation-Based Modeling of Capillary-Driven Flow in Porous Systems. *Langmuir* **2021**, *37*, 1623–1636.

25. Wenzel, R. N. Resistance of Solid Surfaces to Wetting by Water. *Ind. Eng. Chem.* **1936**, *28*, 988–994.

26. Cassie, A.; Baxter, S. Wettability of Porous Surfaces. *Trans. Faraday Soc.* **1944**, *40*, 546–551.

27. Quéré, D. Wetting and Roughness. *Annu. Rev. Mater. Res* **2008**, *38*, 71–99.

28. Roché, M.; Talini, L.; Verneuil, E. Complexity in Wetting Dynamics. *Langmuir* **2024**, *40*, 2830–2848.

29. Joanny, J.F. and de Gennes, P.G., A Model for Contact Angle Hysteresis. *J. Chem. Phys.* **1984**, *81*, 552–562.

30. Villegas, M.; Zhang, Y.; Abu Jarad, N.; Soleymani, L.; Didar, T. F. Liquid-Infused Surfaces: A Review of Theory, Design, and Applications. *ACS Nano* **2019**, *13*, 8517–8536.

31. Lafuma, A.; Quéré, D. Superhydrophobic States. *Nat. Mater.* **2003**, *2*, 457–460.

32. Kim, J.; Moon, M.-W.; Kim, H.-Y. Capillary rise in superhydrophilic rough channels. *Phys. Fluids* **2020**, *32*, art. no. 032105.

33. Panter, J. R.; Konicek, A. R.; King, M. A.; Jusufi, A.; Yeganeh, M. S.; Kusumaatmaja, H. Rough capillary rise. *Comm. Phys.* **2023**, *6*, art. no. 44.

34. Rolison, D. R. Catalytic Nanoarchitectures–the Importance of Nothing and the Unimportance of Periodicity. *Science* **2003**, *299*, 1698–1701.

35. Gommes, C. J. Stochastic models of disordered mesoporous materials for small-angle scattering analysis and more. *Microporous Mesoporous Mater.* **2018**, *257*, 62–78.

36. Gommes, C. J.; Roberts, A. P. Stochastic Analysis of Capillary Condensation in Disordered Mesopores. *Phys. Chem. Chem. Phys.* **2018**, *20*, 13646–13659.

37. Wang, C.; Mehmani, Y.; Xu, K. Capillary Equilibrium of Bubbles in Porous Media. *Proc. Natl. Acad. Sci. U. S. A.* **2021**, *118*, art. no. e2024069118.

38. de Gennes, P. G. Wetting: Statics and Dynamics. *Rev. Mod. Phys.* **1985**, *57*, 827–863.

39. Bonn, D.; Eggers, J.; Indekeu, J.; Meunier, J. Wetting and Spreading. *Rev. Mod. Phys.* **2009**, *81*, 739–805.

40. Kavokine, N.; Netz, R. R.; Bocquet, L. Fluids at the Nanoscale: From Continuum to Subcontinuum Transport. *Annu. Rev. Fluid Mech.* **2021**, *53*, 377–410.

41. Israelachvili, J. *Intermolecular and Surface Forces*; Academic Press, 2011.

42. Gravelle, S.; Ybert, C.; Bocquet, L.; Joly, L. Anomalous Capillary Filling and Wettability Reversal in Nanochannels. *Phys. Rev. E* **2016**, *93*, art. no. 033123.

43. Holt, J. K.; Park, H. G.; Wang, Y.; Stadermann, M.; Artyukhin, A. B.; Grigoropoulos, C. P.; Noy, A.; Bakajin, O. Fast Mass Transport Through Sub-2-Nanometer Carbon Nanotubes. *Science* **2006**, *312*, 1034–1037.

44. Huang, D. M.; Sendner, C.; Horinek, D.; Netz, R. R.; Bocquet, L. Water Slippage Versus Contact Angle: A Quasiuniversal relationship. *Phys. Rev. Lett.* **2008**, *101*, art. no. 226101.

45. Chen, X.; Ma, R.; Li, J.; Hao, C.; Guo, W.; Luk, B.; Li, S. C.; Yao, S.; Wang, Z. Evaporation of Droplets on Superhydrophobic Surfaces: Surface Roughness and Small Droplet Size Effects. *Physical Review Letters* **2012**, *109*, 116101.

46. Král, P.; Shapiro, M. Nanotube Electron Drag in Flowing Liquids. *Phys. Rev. Lett.* **2001**, *86*, 131–134.

47. Bocquet, L.; Charlaix, E. Nanofluidics, from Bulk to Interfaces. *Chem. Soc. Rev.* **2010**, *39*, 1073–1095.

48. Vincent, O.; Marguet, B.; Stroock, A. D. Imbibition Triggered by Capillary Condensation in Nanopores. *Langmuir* **2017**, *33*, 1655–1661.

49. Clavaud, C.; Maza-Cuello, M.; Frétigny, C.; Talini, L.; Bickel, T. Modification of the Fluctuation Dynamics of Ultrathin Wetting Films. *Phys. Rev. Lett.* **2021**, *126*, art. no. 228004.

50. Zhao, C.; Zhang, Z.; Si, T. Fluctuation-driven instability of nanoscale liquid films on chemically heterogeneous substrates. *Phys. Fluids* **2023**, *35*, art. no. 072016.

51. Yang, Q.; Sun, P.; Fumagalli, L.; Stebunov, Y.; Haigh, S.; Zhou, Z.; Grigorieva, I.; Wang, F.; Geim, A. Capillary condensation under atomic-scale confinement. *Nature* **2020**, *588*, 250–253.

52. Seveno, D.; Blake, T. D.; De Coninck, J. Young's Equation at the Nanoscale. *Phys. Rev. Lett.* **2013**, *111*, art. no. 096101.

53. Dujardin, E.; Ebbesen, T.; Hiura, H.; Tanigaki, K. Capillarity and Wetting of Carbon Nanotubes. *Science* **1994**, *265*, 1850–1852.

54. Tas, N. R.; Haneveld, J.; Jansen, H. V.; Elwenspoek, M.; van den Berg, A. Capillary Filling Speed of Water in Nanochannels. *Appl. Phys. Lett.* **2004**, *85*, 3274–3276.

55. Mattia, D.; Gogotsi, Y. Review: Static and Dynamic Behavior of Liquids Inside Carbon Nanotubes. *Microfluid. Nanofluid.* **2008**, *5*, 289–305.

56. Xie, Q.; Alibakhshi, M. A.; Jiao, S.; Xu, Z.; Hempel, M.; Kong, J.; Park, H. G.; Duan, C. Fast Water Transport in Graphene Nanofluidic Channels. *Nat. Nanotechnol.* **2018**, *13*, 238–245.

57. Gommes, C. J.; Jaksch, S.; Frielinghaus, H. Small-Angle Scattering for Beginners. *J. Appl. Crystallogr.* **2021**, *54*, 1832–1843.

58. Glatter, O. *Scattering Methods and their Application in Colloid and Interface Science*; Elsevier, 2018.

59. Pekala, R. W. Organic Aerogels from the Polycondensation of Resorcinol with Formaldehyde. *J. Mater. Sci.* **1989**, *24*, 3221–3227.

60. Al-Muhtaseb, S. A.; Ritter, J. A. Preparation and Properties of Resorcinol-Formaldehyde Organic and Carbon Gels. *Adv. Mater.* **2003**, *15*, 101–114.

61. Elkhatat, A. M.; Al-Muhtaseb, S. A. Advances in Tailoring Resorcinol-Formaldehyde Organic and Carbon Gels. *Adv. Mater.* **2011**, *23*, 2887–2903.

62. Lee, J.-H.; Park, S.-J. Recent Advances in Preparations and Applications of Carbon Aerogels: A Review. *Carbon* **2020**, *163*, 1–18.

63. Moreno-Castilla, C.; Maldonado-Hódar, F. Carbon Aerogels for Catalysis Applications: An Overview. *Carbon* **2005**, *43*, 455–465.

64. Biener, J.; Stadermann, M.; Suss, M.; Worsley, M. A.; Biener, M. M.; Rose, K. A.; Baumann, T. F. Advanced Carbon Aerogels for Energy Applications. *Energy Environ. Sci.* **2011**, *4*, 656–667.

65. Piedboeuf, M.-L. C.; Léonard, A. F.; Reichenauer, G.; Balzer, C.; Job, N. How do the micropores of carbon xerogels influence their electrochemical behavior as anodes for lithium-ion batteries? *Microporous Mesoporous Mater.* **2019**, *275*, 278–287.

66. Gommes, C. J.; Chaltin, F. c. The electrical impedance of carbon xerogel hierarchical electrodes. *Electrochimica Acta* **2022**, *433*, 141203.

67. Job, N.; Pirard, R.; Marien, J.; Pirard, J.-P. Porous Carbon Xerogels with Texture Tailored by pH Control During Sol-Gel Process. *Carbon* **2004**, *42*, 619–628.

68. Hanzawa, Y.; Kaneko, K.; Pekala, R. W.; Dresselhaus, M. S. Activated Carbon Aerogels. *Langmuir* **1996**, *12*, 6167–6169.

69. Broekhoff, C. J. P.; de Boer, J. H. Studies on Pore Systems in Catalysts. IX. Calculation of Pore Distributions from the adsorption Branch of Nitrogen Sorption Isotherms in the Case of Open Cylindrical Pores A. Fundamental Equations. *J. Catal.* **1967**, *9*, 8–14.

70. Gregg, S.; Sing, K. *Adsorption, Surface Area and Porosity*; Academic Press: London, 1982.

71. Galarneau, A.; Villemot, F.; Rodriguez, J.; Fajula, F.; Coasne, B. Validity of the t-plot Method to Assess Microporosity in Hierarchical Micro/Mesoporous Materials. *Langmuir* **2014**, *30*, 13266–13274.

72. Rutherford, S. Modeling Water Adsorption in Carbon Micropores: Study of Water in Carbon Molecular Sieves. *Langmuir* **2006**, *22*, 702–708.

73. Bras, W.; Dolbnya, I.; Detollenaere, D.; Van Tol, R.; Malfois, M.; Greaves, G.; Ryan, A.; Heeley, E. Recent Experiments on a Combined Small-Angle/Wide-Angle X-Ray Scattering Beam Line at the ESRF. *J. Appl. Crystallogr.* **2003**, *36*, 791–794.

74. Gommes, C. J.; Goderis, B. CONEX, a Program for Angular calibration and Averaging of Two-Dimensional Powder Scattering Patterns. *J. Appl. Crystallogr.* **2010**, *43*, 352–355.

75. Huang, T.; Toraya, H.; Blanton, T.; Wu, Y. X-ray powder diffraction analysis of silver behenate, a possible low-angle diffraction standard. *J. Appl. Crystallogr.* **1993**, *26*, 180–184.

76. Seltzer, S. X-ray Form Factor, Attenuation and Scattering Tables. NIST Standard Reference Database 66, 1995; `http://www.nist.gov/pml/data/ffast/index.cfm`, Accessed on 29 March 2023.

77. Lin, C.; Ritter, J. A. Carbonization and activation of sol-gel derived carbon xerogels. *Carbon* **2000**, *38*, 849–861.

78. Hanzawa, Y.; Kaneko, K. Lack of a Predominant Adsorption of Water Vapor on Carbon Mesopores. *Langmuir* **1997**, *13*, 5802–5804.

79. Alcaniz-Monge, J.; Linares-Solano, A.; Rand, B. Water Adsorption on Activated Carbons: Study of Water Adsorption in Micro- and Mesopores. *J. Phys. Chem. B* **2001**, *105*, 7998–8006.

80. Wiener, M.; Reichenauer, G. Microstructure of porous carbons derived from phenolic resin - Impact of annealing at temperatures up to 2000°C analyzed by complementary characterization methods. *Microporous Mesoporous Mater.* **2015**, *203*, 116–122.

81. Debye, P.; Bueche, A. Scattering by an Inhomogeneous Solid. *J. Appl. Phys.* **1949**, *20*, 518–525.

82. Perret, R.; Ruland, W. X-Ray Small-Angle Scattering of Non-Graphitizable Carbons. *J. Appl. Crystallogr.* **1968**, *1*, 308–313.

83. Scherdel, C.; Reichenauer, G. Carbon Xerogels Synthesized via Phenol-Formaldehyde gels. *Microporous Mesoporous Mater.* **2009**, *126*, 133–142.

84. Gommes, C. J.; Roberts, A. P. Structure Development of Resorcinol-Formaldehyde Gels: Microphase Separation or Colloid Aggregation. *Phys. Rev. E* **2008**, *77*, 041409.

85. Jafta, C. J.; Petzold, A.; Risse, S.; Clemens, D.; Wallacher, D.; Goerigk, G.; Ballauff, M. Correlating Pore Size and Shape to Local Disorder in Microporous Carbon: A Combined Small Angle Neutron and X-Ray Scattering Study. *Carbon* **2017**, *123*, 440–447.

86. Ciccariello, S.; Riello, P.; Benedetti, A. Small-Angle Scattering Behavior of Thread-Like and Film-Like Systems. *J. Appl. Crystallogr.* **2016**, *49*, 260–276.

87. Happel, J. Viscous Flow in Multiparticle Systems: Slow Motion of Fluids Relative to Beds of Spherical Particles. *AIChE J.* **1958**, *4*, 197–201.

88. Katz, A.; Thompson, A. Quantitative prediction of permeability in porous rock. *Phys. Rev. B* **1986**, *34*, 8179–8181.

89. Abdallah, B.; Willot, F.; Jeulin, D. Stokes Flow Through a Boolean Model of Spheres: Representative Volume Element. *Transp. Porous Media* **2015**, *109*, 711–726.

90. Xu, P.; Yu, B. Developing a new form of permeability and Kozeny-Carman constant for homogeneous porous media by means of fractal geometry. *Adv. Water Resour.* **2008**, *31*, 74–81.

91. Ozgumus, T.; Mobedi, M.; Ozkol, U. Determination of Kozeny Constant Based on Porosity and Pore to Throat Size Ratio in Porous Medium with Rectangular Rods. *Eng. Appl. Comput. Fluid Mech.* **2014**, *8*, 308–318.

92. Moone, L.; Donners, M.; van Durme, K.; Okhrimenko, D.; van Benthem, R.; Tuinier, R.; Esteves, A. Surface Characteristics of Phenolic Resin Coatings. *Surf. Interf.* **2024**, *45*, art. no. 103840.

93. Bico, J.; Thiele, U.; Quéré, D. Wetting of Textured Surfaces. *Colloids Surf., A* **2002**, *206*, 41–46.

94. Drelich, J.; Chibowski, E.; Meng, D. D.; Terpilowski, K. Hydrophilic and Superhydrophilic Surfaces and Materials. *Soft Matter* **2011**, *7*, 9804–9828.

95. Li, Z.; Wang, Y.; Kozbial, A.; Shenoy, G.; Zhou, F.; McGinley, R.; Ireland, P.; Morganstein, B.; Kunkel, A.; Surwade, S. P.; Li, L.; Liu, H. Effect of Airborne Contaminants on the Wettability of Supported Graphene and Graphite. *Nat. Mater.* **2013**, *12*, 925–931.

96. Mücksch, C.; Rösch, C.; Müller-Renno, C.; Ziegler, C.; Urbassek, H. M. Consequences of Hydrocarbon Contamination for Wettability and Protein Adsorption on Graphite Surfaces. *J. Phys. Chem. C* **2015**, *119*, 12496–2501.

97. Kärger, J.; Ruthven, D. M. Diffusion in Nanoporous Materials: Fundamental Principles, Insights and Challenges. *New J. Chem.* **2016**, *40*, 4027–4048.

98. Heinke, L.; Kortunov, P.; Tzoulaki, D.; Kärger, J. Exchange Dynamics at the Interface of Nanoporous Materials with their Surroundings. *Phys. Rev. Lett.* **2007**, *99*, 228301.

99. Tzoulaki, D.; Heinke, L.; Lim, H.; Li, J.; Olson, D.; Caro, J.; Krishna, R.; Chmelik, C.; Kärger, J. Assessing Surface Permeabilities from Transient Guest Profiles in Nanoporous Host Materials. *Angew. Chem. Int. Ed.* **2009**, *48*, 3525–3528.

100. Sastre, G.; Kärger, J.; Ruthven, D. M. Diffusion Path Reversibility Confirms Symmetry of Surface Barriers. *J. Phys. Chem. C* **2019**, *123*, 19596–19601.

101. Jentys, A.; Mukti, R. R.; Lercher, J. A. On the Sticking Probability of Aromatic Molecules on Zeolites. Comment on Sticking Probability on Zeolites. *J. Phys. Chem. B* **2006**, *110*, 17691–17693.

102. Adamson, A. W. *A Textbook of Physical Chemistry*; Academic Press: New York, 1979.

103. Bird, R. B.; Stewart, W. E.; Lightfoot, E. N. *Transport Phenomena*, 2nd ed.; Wiley, 2002.

104. Misra, R. P.; Blankschtein, D. Insights on the Role of Many-Body Polarization Effects in the Wetting of Graphitic Surfaces by Water. *J. Phys. Chem. C* **2017**, *121*, 28166–28179.

Graphical TOC Entry